Surface-Acoustic-Wave Waveguides for Radio Frequency Signal Processing

Masashi Yamagata, *Member, IEEE*, Ning Cao, Demis D. John, *Member, IEEE*, and Hossein Hashemi, *Fellow, IEEE*

***Abstract*— The large velocity of electromagnetic waves makes the design of waveguide structures such as couplers and delay lines at radio frequencies (RFs) prohibitively large for chip-scale implementation. In contrast, acoustic waves have velocities that are many orders of magnitude smaller. Thus, with the use of acoustic waves, RF waveguides become possible. In this article, the waveguiding of sub-1-GHz surface acoustic waves (SAWs) on 128° Y-cut lithium niobate ($LiNbO_3$) is examined with demonstrations of straight waveguides, waveguide bends, and coupled waveguides. Furthermore, an electroacoustic variable phase shifter based on an SAW waveguide on a bonded 128° Y-cut $LiNbO_3$ on silicon is demonstrated. Finally, an all-acoustic bidirectional RF phased array front end is demonstrated. The structures shown in this work can be implemented in commercial SAW foundries resulting in low-cost compact realizations of SAW microwave signal processing structures.**

***Index Terms*— Lithium niobate ($LiNbO_3$), phased array, radio frequency (RF), surface acoustic wave (SAW), waveguides.**

I. Introduction

SURFACE-acoustic-wave (SAW) devices have long been used in communication systems for their low-loss, high selectivity, and small form factors [1], [2]. While they are known for their filtering capabilities, they have been used in oscillators, convolvers, couplers, and compressors [3], [4], [5], [6]. They are also finding uses beyond radio frequency (RF) wireless devices and into areas such as microfluidics, sensors, superconducting circuits, and more [7].

SAWs are also used for delay lines requiring several microseconds of delay as they can be obtained much more compactly in the acoustic domain due to their low wave velocity, allowing for a low-loss delay line compared to electromagnetic counterparts [2]. A calculation of a microstrip line using FR-4 at 600 MHz resulted in a loss per delay of about 600 dB/μs [8]. Even with low-loss silicon photonic waveguides, the measured loss is about 250 dB/μs [9]. Acoustic delay lines, however, have been demonstrated with a loss of 2.07 dB/μs at 300 MHz using a suspended X-cut lithium niobate ($LiNbO_3$) [10]. However, depending on the delay required, acoustic delay lines can still span several millimeters in length. For example, a 10-μs delay using 128° Y-cut X-propagating $LiNbO_3$ (often denoted as 128° YX $LiNbO_3$), with an SAW velocity of 3979 m/s, will require close to 40 mm in length. Such a long delay line can experience an excessive loss due to diffractive losses experienced by SAWs [1]. The diffractive losses can be minimized by confining the SAW in a waveguide structure. SAW waveguides can also be used to meander the delay line by incorporating waveguide bends, maintaining a compact size.

The confinement of the SAW in waveguides can also guide the SAW in the presence of the beam steering effect [2]. Due to the anisotropy of piezoelectric materials, the SAW power propagates in a direction that is not perpendicular to the face of the interdigital transducer (IDT), whereas the wavefronts are always parallel to it. In other words, the SAW Poynting vector is not parallel to the wavevector. If IDTs were placed across from each other in this instance, excessive loss will be experienced as the SAW will propagate at an angle and away from the output IDT. Confining the SAW in a waveguide will mitigate the losses experienced due to the beam steering effect.

In addition to delay lines, SAW waveguide structures can be used to realize more complex and interesting signal processing functions at RFs. Specifically, modulating the acoustic velocity through electrical means enables all-acoustic variable phase shifters, variable delay elements, and beamformers. An interesting application of a variable delay element is in self-interference cancellation in full-duplex wireless systems [11]. In a full-duplex wireless system, some of the transmitter (Tx) leakage to the receiver (Rx) may experience a significant delay due to reflections in the environment. Self-interference cancellation approaches in the electronic domain may suffer due to limited bandwidth, loss, and poor dynamic range while consuming power. On the other hand, obtaining nanoseconds of delay in the electromagnetic domain is not trivial and requires a significant area at RFs. Acoustic domain variable delay lines are promising as large delays are possible in the acoustic domain due to the relatively low propagation velocity [10]. However, while acoustic delay line structures themselves may possess wideband capabilities, the bandwidth

Manuscript received 28 April 2022; revised 31 July 2022; accepted 22 September 2022. Date of publication 23 November 2022; date of current version 6 March 2023. This work was supported in part by the Semiconductor Research Corporation Joint University Microelectronics Program (SRC JUMP) under the ComSenTer and in part by the NSF under the SpecEES program. *(Corresponding author: Masashi Yamagata.)*

Masashi Yamagata and Hossein Hashemi are with the Ming Hsieh Department of Electrical and Computer Engineering, University of Southern California, Los Angeles, CA 90089 USA (e-mail: myamagat@usc.edu; hosseinh@usc.edu).

Ning Cao and Demis D. John are with the Department of Electrical and Computer Engineering, University of California at Santa Barbara, Santa Barbara, CA 93106 USA (e-mail: ningcao@ucsb.edu; demis@ucsb.edu).

Color versions of one or more figures in this article are available at https://doi.org/10.1109/TMTT.2022.3222395.

Digital Object Identifier 10.1109/TMTT.2022.3222395

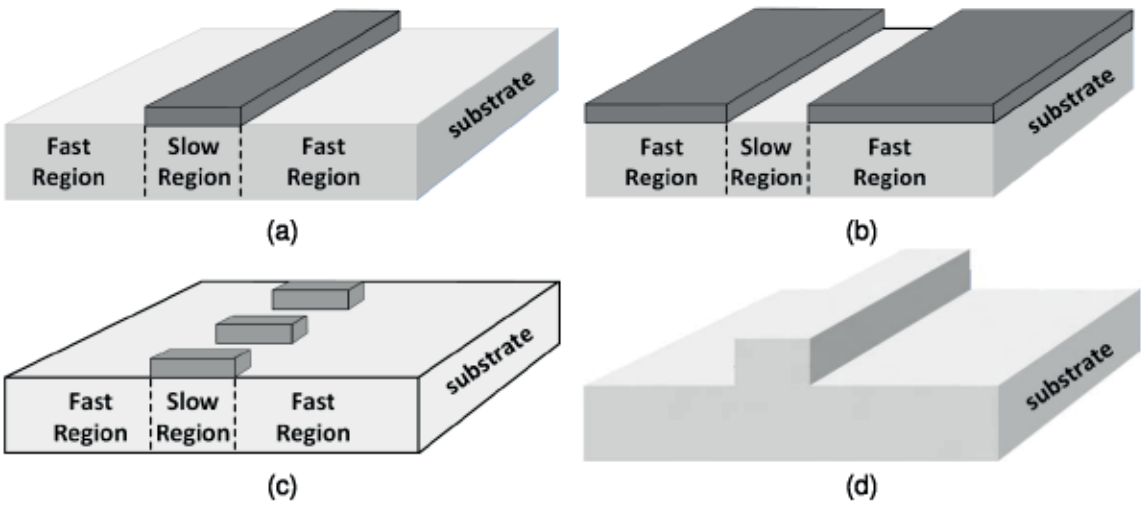

Fig. 1. Different waveguide configurations for SAWs. (a)–(c) Examples of overlay-type waveguides. (d) Topographic waveguide.

of a variable acoustic delay line may be limited by the bandwidth of the IDT.

This work explores SAW waveguide structures, focusing on the guiding of Rayleigh waves and demonstrating waveguide structures at RFs using 128° YX $LiNbO_3$. Section II covers the principles and simulations of SAW waveguides including straight, bent, and coupled waveguides. Straight waveguides, waveguide bends, and directional couplers for SAW have been studied and implemented in previous works, and this work looks to reopen SAW waveguides in a proof of concept for complex integration of RF systems [12], [13], [14], [15]. Section III covers the principles and design guidelines for electroacoustic variable phase shifters. Section IV summarizes the fabrication steps for SAW waveguides. Section V illustrates several implementations of various forms of overlay SAW waveguides using aluminum (Al), tungsten (W), and gold (Au) metallizations as well as electroacoustic variable phase shifters and an all-acoustic bidirectional RF phased array front end. Conclusions are presented in Section VI.

II. SAW Waveguides

A. Background

Interest in the waveguiding of SAWs can be found in papers dating back to the 1960s [12], [13], [16], [17]. An SAW waveguide can have many shapes and forms. In the most general sense, an SAW waveguide can be designed by adding material on to the piezoelectric substrate or by removal of parts of the piezoelectric substrate, as shown in Fig. 1 [13]. The waveguides in the figure fall into overlay-type waveguides, where a material is added to the piezoelectric substrate to create the confinement region [Fig. 1(a)–(c)] or topographic waveguides [Fig. 1(d)] [14], [18], [19], [20]. For the overlay-type SAW waveguides in Fig. 1(a) and (c), a material is placed over the confinement region, mass loading the atoms in the region. This causes the atoms to move slower in the confinement region, creating a velocity differential between the waveguide region and the surrounding region. The waveguide region in effect will have a higher index of refraction and thus confines the SAW in the slow velocity region. On the other hand, in the overlay waveguide of Fig. 1(b), a material that has a faster acoustic velocity compared to the substrate is placed over the "cladding" region or the region outside of the confinement region. This creates an SAW velocity differential by increasing the velocity in the cladding region and confining the SAW in the slow region.

Let us consider the example of realizing a compact SAW delay line for applications such as phased arrays and self-interference cancellers. IDTs are commonly used to convert the electrical signals to acoustic waves and vice versa. In principle, two IDTs can be placed far apart to realize the required delay line [Fig. 2(a)]. However, the SAW beam divergence and the nonstraight beam propagation, due to the anisotropy of the material, result in small, collected power at the second IDT. Alternatively, an SAW waveguide created by overlaying metal on the piezoelectric material between the IDTs can help confine the SAW and improve the propagation loss [Fig. 2(b)]. Finally, meandered waveguides enabled by a combination of straight and bent waveguides can reduce the overall footprint of the delay line [Fig. 2(c)].

B. Metal Overlaid SAW Waveguides

The primary substrate material used for this study is a 128° Y-cut $LiNbO_3$ with the main propagation direction being in the x-direction. The 128° YX $LiNbO_3$ has a relatively high piezoelectric coupling coefficient as well as lower bulk wave generation [2]. An SAW generated on 128° YX $LiNbO_3$ also does not have any beam steering effects that can have a detrimental effect on the performance of the propagating SAW. In order to keep the fabrication simple and minimal, only one mask was used in this work. This limited the structure to an overlay-type waveguide structure such as shown in Fig. 1(a) and (c). It also constrained the overlay material to be the same material and thickness as the IDTs. Note that these constraints are not necessary, but they ensure that the structures can be easily fabricated in commercial SAW foundries. With this limitation in mind, aluminum, tungsten, and gold were used as the metallization material in this investigation. Aluminum is a light metal with a mass density of about

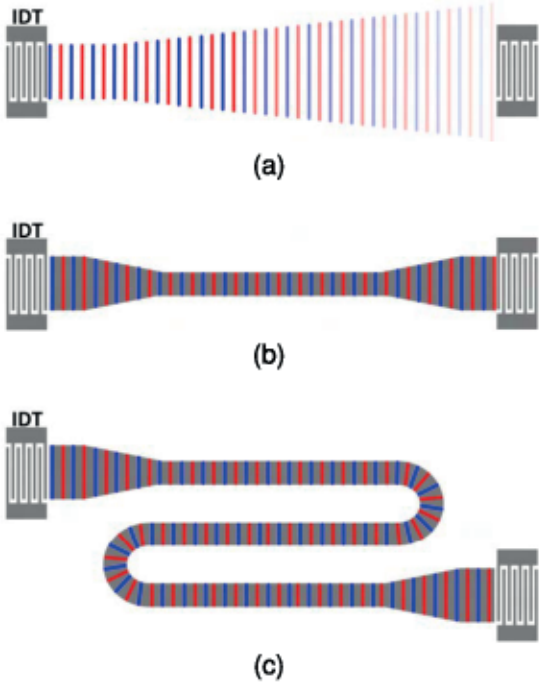

Fig. 2. (a) Long, unguided delay line with the SAW experiencing the beamforming effect. (b) Long, guided delay line with confinement of SAW. (c) Long, guided meandered delay line to reduce overall footprint.

TABLE I
OVERLAY METAL PROPERTIES[1]

Metal	Al	Au	W
Mass Density (kg/m^3)	2700	19320	19250
Young's Modulus (GPa)	68	77	400
Poisson's Ratio	0.36	0.42	0.28
Electrical Conductivity (S/m)	$3.7\text{x}10^7$	$4.545\text{x}10^7$	$1.77\text{x}10^7$

[1] www.matweb.com

2700 kg/m^3, while tungsten and gold are heavier metals with both having mass densities around 19 300 kg/m^3 [21], [22], [23]. While tungsten and gold have similar mass densities, the two differ in their electrical conductivities and stiffness properties, with gold being more electrically conductive and having a smaller Young's modulus compared to tungsten. The properties between the metals are summarized in Table I.

The SAW velocity of the overlay waveguides versus the metal thickness for the three metals has been calculated using a 3-D model in COMSOL Multiphysics with the piezoelectric multiphysics included. The results are plotted in Fig. 3. The SAW velocities were calculated from the simulated eigenfrequencies for a metallized surface. As expected from the different mass densities, aluminum only has a small effect on the SAW velocity, indicating that a waveguide designed using aluminum will most likely not confine the SAW well compared to waveguides constructed with the heavier tungsten or gold. Also, from simulations, it seems like the difference in Young's modulus between tungsten and gold plays a large role in gold showing a larger change in velocity with metal thickness compared to tungsten. Considering the SAW velocity

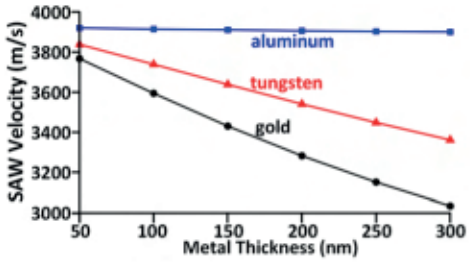

Fig. 3. Simulated SAW velocities for aluminum, tungsten, and gold overlay waveguides with $\lambda = 6.56$ μm.

and the fabrication lithography limits for resolving the IDT periodicity, a thickness of 100 nm was chosen for the target frequency of around 600 MHz.

The width of the waveguide is determined by analyzing dispersion curves of the waveguide structure. The dispersion curves with 100-nm-thick gold metallization were calculated from eigenfrequency simulations using Floquet boundary conditions, as shown in Fig. 4(a). A perfectly matched layer is used for the bottom of the structure, while low-reflecting boundary conditions are applied to the transverse faces. A floating electrical boundary condition is applied to the metal. Even- and odd-mode eigenfrequencies for the Rayleigh mode and higher surface modes propagating in the waveguide confinement region were recorded and their respective velocities were calculated. The results for a few waveguide widths and for a wavelength of 6.56 μm are shown in Fig. 4(b)–(d). The red solid horizontal line represents the desired Rayleigh mode velocity that would be excited from an IDT. Due to the difference in the mass loading effect from a grating structure of an IDT and a solid metal of the waveguide, the Rayleigh mode velocities will be different between the two different structures. The gray curve represents the Rayleigh mode of the waveguide, while the cyan and black curves represent higher order modes. A close-up view near the wavenumber $2\pi/\lambda$ is also shown. From the plots, it can be seen that for the 3-μm waveguide width, the desired Rayleigh mode is not supported by the waveguide, while it is supported for the 6- and 12-μm waveguide widths. However, a higher order surface mode is also supported for the 12-μm waveguide width, which is not desirable as it can lead to a higher propagation loss of the fundamental mode. Therefore, based on the dispersion curves, a waveguide with a width of 6 μm was chosen for the SAW waveguide design.

A 3-D frequency-domain simulation in COMSOL with piezoelectric multiphysics was performed to evaluate the confinement of the waveguide for different overlay materials of width of 6 μm and thickness of 100 nm. The SAW was generated using simplified IDT structures with a 6-μm aperture width and a metal thickness of 100 nm. The electrical loss of the metals was not included in the simulation. The ratio of the strain energy under the overlay metal (waveguide region) over the entire strain energy (directly underneath and outside of the overlay metal) is computed as the confinement factor. The calculated confinements for gold, tungsten, and aluminum are 79%, 71%, and 47%, respectively, confirming the previous conclusions.

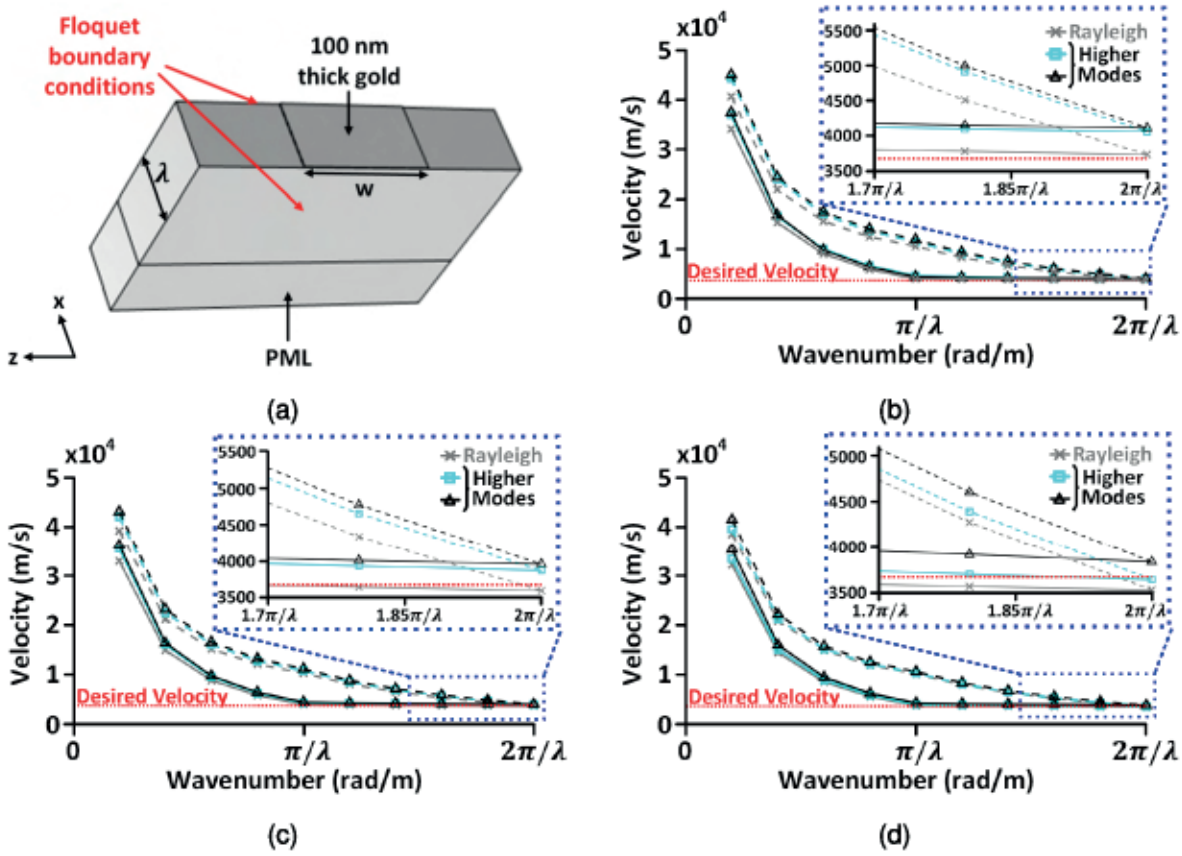

Fig. 4. Simulated dispersion curves for gold overlay SAW waveguides. (a) Eigenfrequency simulation setup for calculating the dispersion curves. Floquet periodic boundary conditions are applied on both sides of the structure. Dispersion curves for waveguide widths, w, of (b) 3, (c) 6, and (d) 12 μm and for $\lambda = 6.56$ μm are shown. The dotted horizontal red line is the desired SAW velocity. The gray lines are the Rayleigh wave velocities under the waveguide structure, while the cyan and black lines are velocities of higher order modes. The solid lines are velocities for even modes, while the dotted lines are velocities for the odd mode.

C. Interdigital Transducers

The IDT was designed to provide 50-Ω impedance matching, so measurements can be performed without an external impedance matching network. A 3-D COMSOL frequency-domain simulation with piezoelectric multiphysics was used to evaluate the reflection coefficient of a 130-μm-wide, 24-electrode pair standalone IDT. As the structure is large, some accuracy was sacrificed by using a coarser mesh with a minimum size of $\lambda/5$ and a maximum of $\lambda/3$ in order to simulate the structure. The IDT was designed to operate at the acoustic wavelength of 6.56 μm and constructed using 100-nm-thick gold on 128° YX $LiNbO_3$. The simulated S_{11} result is shown in Fig. 5.

D. Waveguide Taper

A waveguide taper is used to mate the wide aperture IDT to the narrower width of the main waveguide, as shown in Fig. 6(a). A 3-D frequency-domain simulation in COMSOL with piezoelectric multiphysics is performed for the linear taper structure. Accuracy was sacrificed in order to simulate this structure as well by using a coarser mesh. A spot frequency-domain simulation was performed to further reduce simulation time. The purpose of the simulation was to capture the trend of the taper loss. Monitors are placed at both ends of the taper and the loss is calculated by taking the ratios of the simulated strain energy at these monitors. The loss of the linear taper across different taper lengths is plotted in Fig. 6(b). A taper length of 1 mm was chosen in the designs throughout this article.

E. Waveguide Bends

Waveguide bends are essential enablers of complex waveguide-based structures. Let us consider a 180° circular waveguide bend shown in Fig. 7(a) along with monitors to calculate the loss from the strain energy difference between the two monitors using COMSOL, similar to the calculation method for the waveguide taper. A 3-D frequency-domain simulation with the piezoelectric effect was performed for both a wavelength and waveguide width of 6 μm and for a gold metallization thickness of 100 nm for several bend radii. A simplified IDT structure with an aperture width of 6 μm is used to generate the SAW. The calculated loss of this 180° circular waveguide bend versus the bend radius using this method is shown in Fig. 7(b). As expected, the loss is larger for smaller bend radii given the limited wave confinement in the waveguide. While the larger bend radius improves confinement in the waveguide, eventually, the propagation loss stemming from the longer path length experienced from the increasing

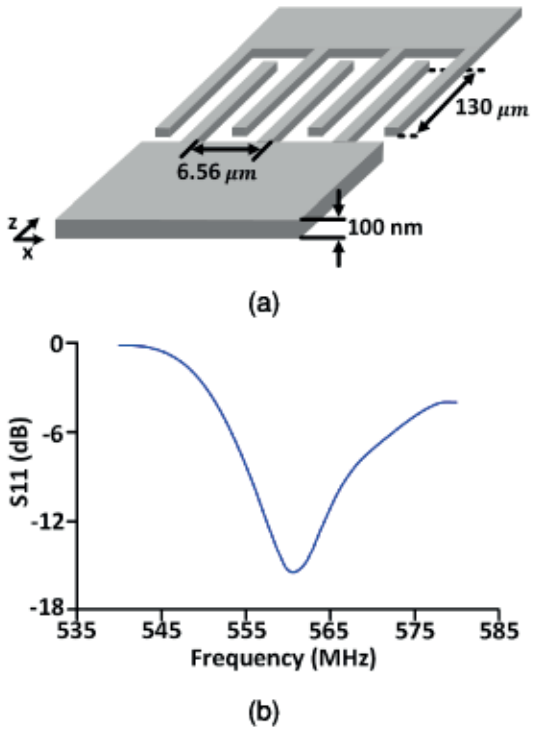

Fig. 5. (a) Drawing of the IDT with aperture width of 130-μm and 100-nm-thick gold electrode pairs. (b) Corresponding 3-D COMSOL simulated S_{11} for 24 electrode pairs.

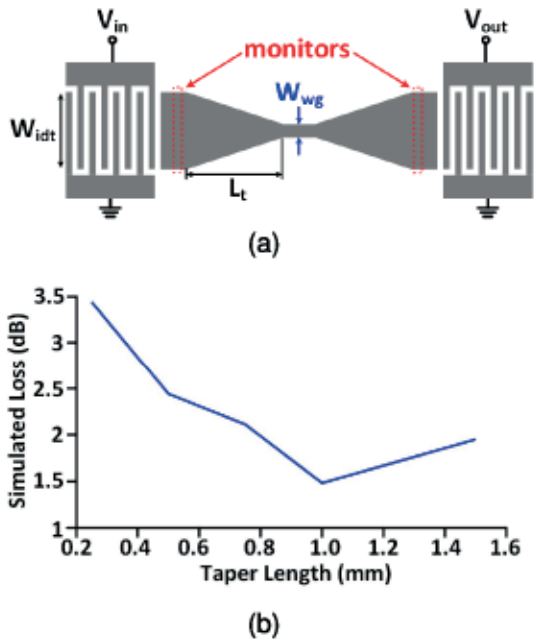

Fig. 6. (a) Waveguide taper simulation setup mating an aperture width of w_{IDT} on to w_{wg}, corresponding to the IDT aperture widths and waveguide aperture widths. (b) Simulated loss for w_{IDT} of 100 μm and w_{wg} of 6 μm over the taper length of L_t.

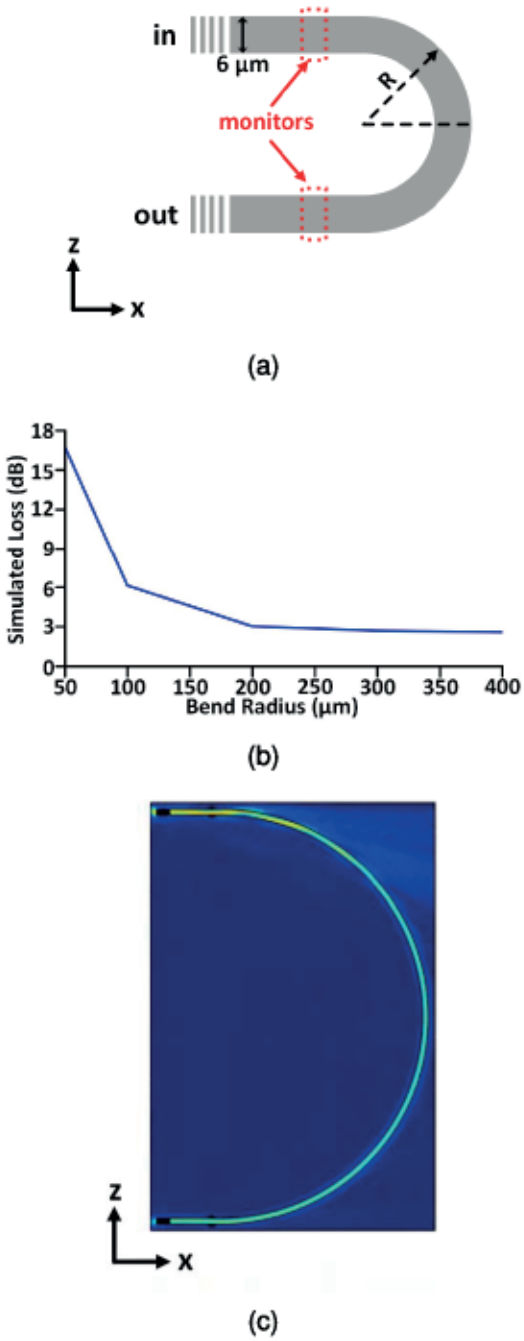

Fig. 7. (a) Simulation setup for analyzing waveguide bends with a waveguide width of 6 μm. (b) Simulation result for 180° bend for $\lambda = 6$ μm and a waveguide width of 6 μm. (c) Total displacement simulation result for 180° bend for a waveguide width of 6 μm and a bend radius of 200 μm.

bend radius will have a detrimental effect on the overall bend loss. Wave confinement through the waveguide bend can be seen in Fig. 7(c), which shows the total displacement of the SAW propagating through a 180° waveguide bend with a radius of 200 μm, a waveguide width of 6 μm, and a 100-nm-thick gold metallization.

F. Coupled Waveguides

Coupled waveguides are commonly used in microwave structures and can be mimicked in the acoustic domain. As expected, the coupling coefficient between two adjacent identical SAW waveguides depends on waveguide lengths and the gap between the waveguides. The coupling length, defined as the length where all the power couples from one waveguide

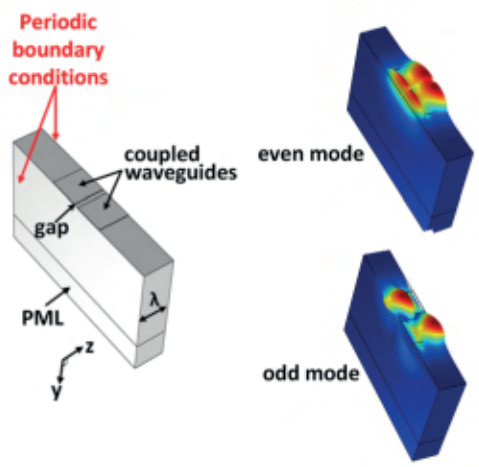

Fig. 8. Eigenfrequency simulation setup (left) and result for even and odd modes (right) for coupled waveguides with $\lambda = 5.64$ μm and a waveguide width of 6 μm.

to another, is calculated by finding the symmetric (even) and antisymmetric (odd) modes of a two-coupled waveguide system using eigenfrequency simulations (Fig. 8) [24]. Periodic boundary conditions were applied to the two faces in the direction of propagation, while low-reflecting boundary conditions were applied to the two transverse faces. A perfectly matched layer is used for the bottom of the structure, while floating electrical boundary conditions are applied to the metals. The even- and odd-mode relative refractive indices are calculated based on the even- and odd-mode eigenfrequencies and subsequently used to calculate the coupling length using

$$L_c = \frac{\lambda}{2\Delta n} \tag{1}$$

where Δn is the difference between the relative refractive indices of the symmetric and antisymmetric modes. Δn can also be expressed in terms of the even mode, odd mode, and free surface velocities as

$$\Delta n = n_{\text{even}} - n_{\text{odd}} = v_{\text{free}} \frac{v_{\text{odd}} - v_{\text{even}}}{v_{\text{even}} v_{\text{odd}}}. \tag{2}$$

The results for an SAW centered near 600 MHz with a 100-nm gold overlay are tabulated in Table II.

The computed coupling lengths in Table II are then further refined using COMSOL 3-D frequency-domain simulations. A structure consisting of two waveguides separated by a gap and excited by a small IDT, as shown in Fig. 9(a). The aperture width of the waveguides is 6 μm and the gap is 1 μm. The vertical displacements between the waveguide and the coupled waveguide are plotted in Fig. 9(b). The difference between the displacement minimums between the waveguide to the coupled waveguide is then evaluated. This distance is the coupling length required for 100% coupling. The coupling length of 127 μm matches well with the calculated coupling length of 135.1 μm using the even and odd eigenfrequencies tabulated in Table II.

III. SAW Variable Phase Shifter Waveguides

Variable phase shifters are essential enablers in RF signal processors such as beamformers and self-interference cancellers. The phase of a propagating wave may be changed by adjusting the propagation velocity.

TABLE II
Calculated Coupled Waveguide Length

gap (μm)	F_{even} (MHz)	F_{odd} (MHz)	n_{even}	n_{odd}	L_c (μm)
1	585.47	596.81	1.0989	1.0781	135.1

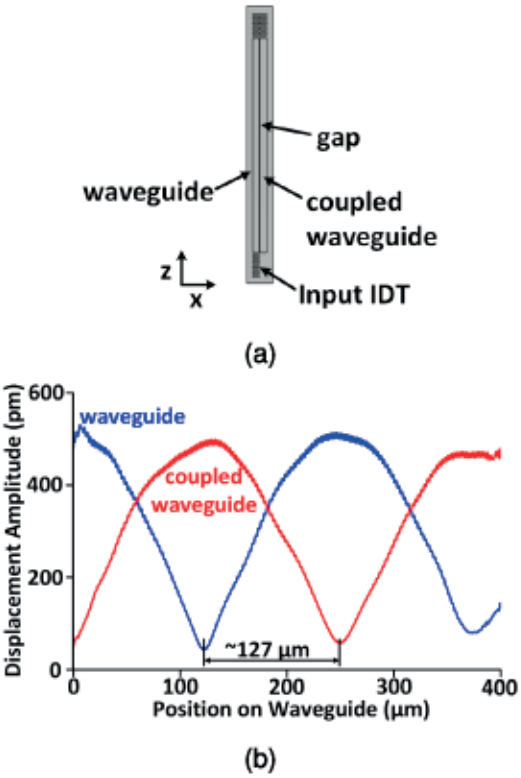

Fig. 9. (a) Waveguide coupler simulation setup. (b) Waveguide coupler vertical displacements for waveguide and coupled waveguide for a gap = 1 μm.

A. Thermal Phase Shifters

As SAW devices are known for having very good temperature stability, it is not surprising that a search for a thermal phase shifter is not very fruitful. The temperature coefficient for the SAW velocity of an x-propagating and z-propagating SAW on 128° Y-cut $LiNbO_3$ (128° YX $LiNbO_3$ and 128° YZ $LiNbO_3$) is -71.3 and -86.3 ppm/°C, respectively [25]. The length of the waveguide to generate a 360° phase shift is calculated by using the equation

$$\Delta\phi = \frac{2\pi L}{\lambda} \frac{dn}{dT} \Delta T \tag{3}$$

where $\Delta\phi$ is the phase change, L is the device length, λ is the SAW wavelength, $(dn)/(dT)$ is the SAW velocity temperature coefficient, and ΔT is the change in temperature [26]. Using (3) and the SAW velocity temperature coefficient of -71.3 ppm/°C, the required lengths of the phase shifter for different temperature differentials were calculated for a 128° YX $LiNbO_3$ and the result is plotted in Fig. 10.

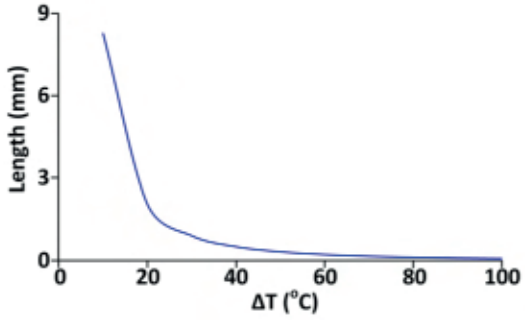

Fig. 10. Plot of phase shifter length versus temperature change.

In order to make the thermal phase shifter have a short length, a large temperature change needs to be generated, resulting in high power consumption. To reduce the power consumption, a phase shifter with a longer length is required. We have experimentally demonstrated a 4-mm-long thermal phase shifter realized using an SAW waveguide on a 128° Y-cut $LiNbO_3$ with 100-nm gold overlay next to a meandered metal creating 2.1 kΩ of resistance as a heating element. The structure requires 322 mW of power to generate a 360° phase shift confirming the inefficiency of thermal phase shifters in today's commercial SAW foundries. It should be noted that the size and power consumption of thermal phase shifters may be reduced by using a meandered waveguide structure with embedded heating elements.

B. Electroacoustic Phase Shifter

The propagation constant of an SAW on a piezoelectric material change as a semiconductor is brought close to the piezoelectric. The underlying reason is the interaction of semiconductor charges with the evanescent fields of the propagating SAW. When an electric field is applied across the combined piezoelectric and semiconductor structure, a depletion region is formed in the semiconductor. The width of the depletion region, which is a function of applied electric field, determines the distance of charges in the semiconductor from the evanescent field of the propagating SAW in the piezoelectric. Hence, a tunable SAW phase shifter may be realized by applying voltage across a combined piezoelectric and semiconductor structure. In 1977, a variable phase shifter using a 34 Ω·cm n-type silicon air gap coupled (with 1000 Å distance) to a YZ-$LiNbO_3$ was demonstrated [27]. In 1982, a ZnO film was deposited on 50-Ω·cm n-type silicon, with 100-nm SiO_2 in between, to create a variable phase shifter. In neither demonstration, the SAW propagates in a waveguide.

In this work, an electrostatic SAW variable phase shifter using an SAW waveguide is demonstrated for the first time. The structure consists of a 5-μm-thick 128° Y-cut $LiNbO_3$ that is bonded onto a 500-μm-thick high-resistivity p-type silicon substrate. A 100-nm-thick gold is used for the IDT and waveguides. The top view of the electroacoustic phase shifter, along with the cross section of the waveguide and substrate structure, is shown in Fig. 11(a) and (b), respectively. The fractional change in the SAW velocity

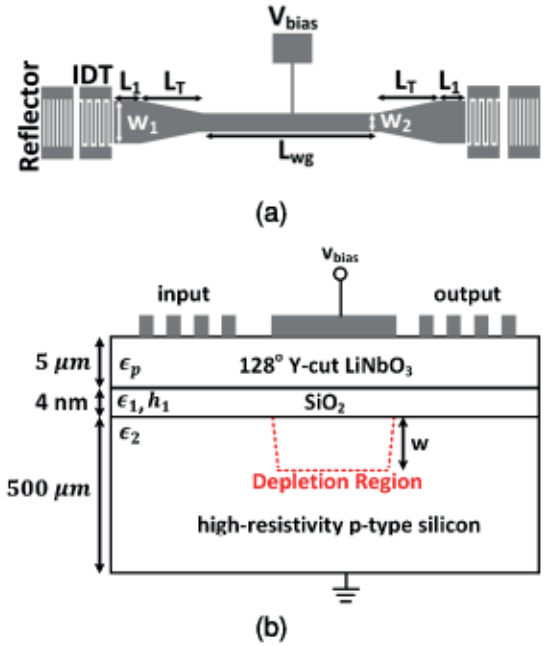

Fig. 11. (a) Top view of the electroacoustic SAW phase shifter. (b) Cross section of an electroacoustic SAW phase shifter.

was calculated using [28]

$$\frac{\Delta v_R}{v} = \left(\frac{\Delta v}{v}\right)\epsilon_1 \frac{1-\frac{\gamma}{\alpha}}{\epsilon_1 + \gamma\epsilon_p} \tag{4}$$

where γ and α are given by

$$\gamma = \frac{\epsilon_2 \tanh(\beta h_1) + \epsilon_1 \tanh(\beta w)}{\epsilon_2 + \epsilon_1 \tanh(\beta h_1)\cdot \tanh(\beta w)} \tag{5}$$

$$\alpha = \frac{\epsilon_1 + \epsilon_2 \tanh(\beta h_1)}{\epsilon_1 \tanh(\beta h_1) + \epsilon_2}. \tag{6}$$

$(\Delta v)/v$, which is the ratio of the velocity difference between an electrically open and short surface over the velocity of the electrically open surface, is calculated from the piezoelectric coupling coefficient, ϵ_1 is the SiO_2 dielectric constant, ϵ_2 is the dielectric constant of silicon, ϵ_p is the dielectric constant of $LiNbO_3$, h_1 is the SiO_2 thickness, β is the SAW propagation constant, and w is the depletion layer width in silicon. The SiO_2 layer is assumed to be around 4 nm in thickness due to the surface oxidation of the silicon prior to the bonding of the $LiNbO_3$ [29]. The waveguide structure is treated similar to a metal–oxide–semiconductor (MOS) capacitor as shown in Fig. 12 and a 1-D COMSOL simulation of an MOS capacitor was performed to evaluate the capacitance of the structure, which is a series combination of the dielectric capacitance from the $LiNbO_3$ layer (C_{LN}) and the depletion capacitance, C_d. The backside of the silicon is electrically grounded, while an electrical potential is applied to the topside of the $LiNbO_3$. The depletion region width is then calculated using

$$w = \frac{\epsilon_{Si}}{C_d} \tag{7}$$

where ϵ_{Si} is the dielectric constant of silicon and C_d is the depletion layer capacitance [30]. The depletion width is

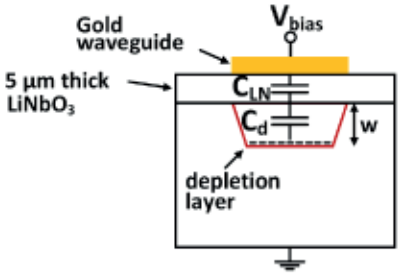

Fig. 12. Waveguide capacitance structure illustrating the depletion region.

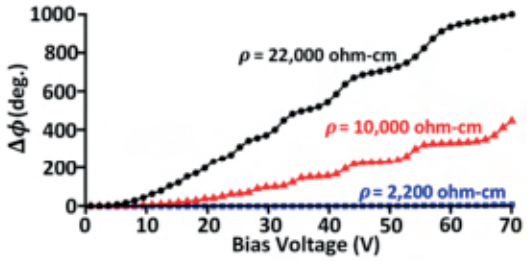

Fig. 13. Calculated shift in phase versus waveguide bias voltage for silicon resistivities of 2200, 10000, and 22000 Ω·cm and phase a shifter length of 6.39 mm.

used to calculate $(\Delta v_R)/v$ using (4), which is then used to calculate the expected phase shift using

$$\Delta\phi = 360^\circ \left(\frac{\Delta v_R}{v}\right)\left(\frac{L_{ps}}{\lambda}\right) \tag{8}$$

where L_{ps} is the length of the phase shifter and λ is the SAW wavelength [31]. Fig. 13 shows the calculated phase shifts for silicon substrate resistivities of 2200, 10000, and 22000 Ω·cm and for a phase shifter length of 6.39 mm versus applied voltage. The exact resistivity of the silicon in the bonded wafer used in this work is unknown except that it is larger than 10000 Ω·cm. The plot shows that a high-resistivity silicon substrate is desirable as it would allow the use of a lower bias voltage to achieve a large phase shift.

IV. Measurements and Discussion

A. Straight Waveguides

The straight SAW waveguides were fabricated on 128° Y-cut $LiNbO_3$ and measurements were obtained by direct RF probing of the devices and measuring the two-port S-parameters using a Keysight N5242A PNA-X network analyzer. The measurements were obtained with no external matching network. A die microphotograph of a straight SAW waveguide with a waveguide width (w) of 6 μm and length (L) of 1 mm is shown in Fig. 14. Single-electrode IDTs were utilized with reflectors placed behind them to reduce the loss from the bidirectionality of the IDT. The IDT was designed with 24 signal-ground finger pairs with an aperture width of 130 μm to provide a good match to 50 Ω. A waveguide taper with a length of 1 mm was used to interface the wide aperture IDT to the narrower aperture of the waveguide [12]. The straight waveguides were fabricated using aluminum, tungsten,

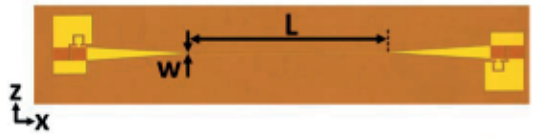

Fig. 14. Die microphotograph of a straight waveguide with aperture width $w = 6$ μm and length $L = 1$ mm.

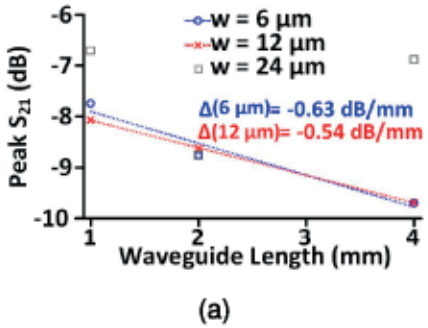

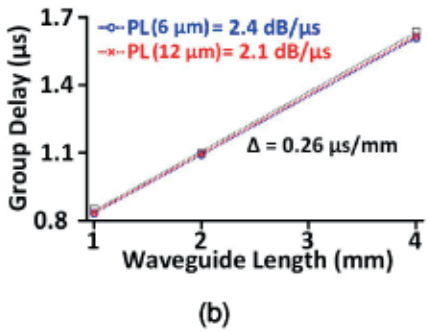

Fig. 15. (a) Peak S_{21} and (b) group delay measurements for straight waveguides fabricated with 100 nm and waveguide widths of 6 μm (blue), 12 μm (red), and 24 μm (gray) for aluminum metallization.

and gold metallizations with a thickness of 100 nm. For gold and aluminum metallizations, 5-nm-thick titanium was used to improve the adhesion between $LiNbO_3$ and the 100-nm-thick metals.

Figs. 15–17 show the peak S_{21} and group delay measurement results for the straight waveguides fabricated using 100-nm-thick aluminum, tungsten, and gold metallizations, respectively, along with their respective linear fit lines. Fig. 15 shows the measurement results for aluminum metallization for a waveguide width of 6, 12, and 24 μm across lengths of 1, 2, and 4 mm. Similar measurement results for tungsten and gold metallizations are shown in Figs. 16 and 17, respectively. As aluminum is lighter with a mass density of about 2700 kg/m^3, compared to about 19300 kg/m^3 for tungsten and gold, it exhibits less of a dampening effect on the propagating SAW and, thus, results in a lower loss [1]. The lower mass loading effect of aluminum also minimizes any acoustic impedance mismatch that is experienced between the IDT, which has a lower mass loading effect due to the grating structure and the solid metal waveguide. It is believed that the 24-μm-wide waveguide experiences excitation of higher

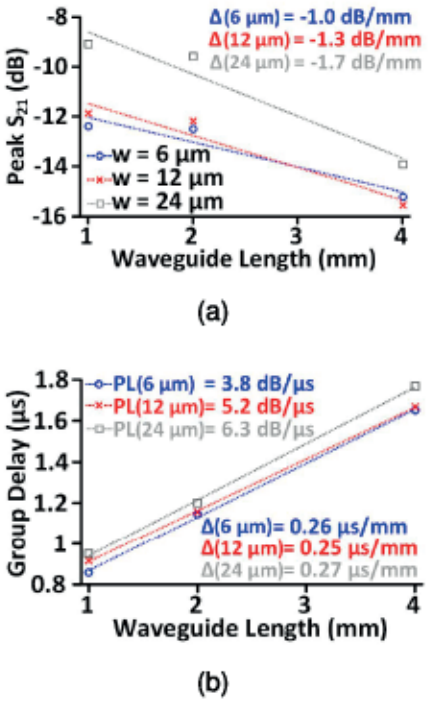

Fig. 16. (a) Peak S_{21} and (b) group delay measurements for straight waveguides fabricated with 100 nm and waveguide widths of 6 μm (blue), 12 μm (red), and 24 μm (gray) for tungsten metallization.

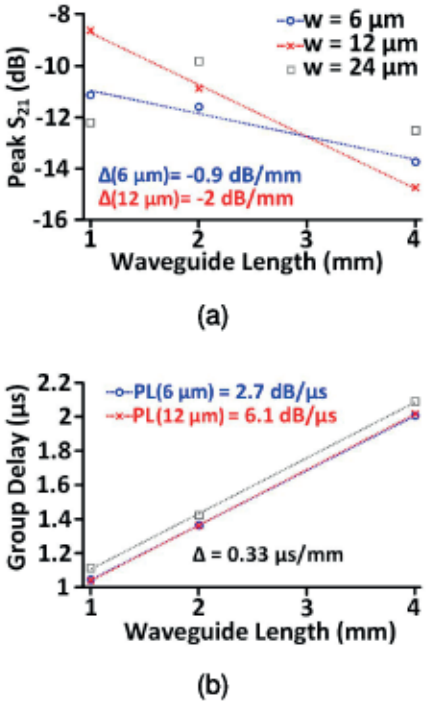

Fig. 17. (a) Peak S_{21} and (b) group delay measurements for straight waveguides fabricated with 100 nm and waveguide widths of 6 μm (blue), 12 μm (red), and 24 μm (gray) for gold metallization.

order modes and, therefore, does not have a good linear fit for aluminum and gold.

It is not clear how much of the electrical conductivity of the metal used in the waveguides contributes to the overall loss. Both aluminum and gold are relatively good electrical conductors (the electrical conductivity of 3.7×10^7 S/m and 4.545×10^7 S/m, respectively), while tungsten is a poorer electrical conductor (1.77×10^7 S/m). However, aluminum is a much lighter metal compared to both gold and tungsten, and tungsten is a much stiffer metal compared to both aluminum and gold as well. Many differences in the metal properties make it difficult to separate the effects of the metal properties and their contribution to the overall loss. Overall, the SAW waveguides demonstrate a low propagation loss in the range of 2.1–6.3 dB/μs. The measurement results show the advantage of SAWs, compared to electromagnetic delay line structures, as the group delay achieved is around 0.3 μs/mm. The 6-μm-wide gold waveguide exhibits a group delay of 0.33 μs/mm and an overall propagation loss of 2.7 dB/μs. On the other hand, a transmission-line-based electromagnetic delay line measured propagation losses of about 990 dB/μs at a frequency of 9.5 GHz, while implementation of a silicon photonic delay line measured delays of about 13.2 ps/mm and an overall propagation loss of about 250 dB/μs [9], [32]. Thus, SAW-based delay lines have delays that are several orders of magnitude larger and propagation losses that are several orders of magnitude smaller than electromagnetic delay lines.

While the straight waveguide measurements show low propagation losses, they do not prove the confinement of wave in the waveguides as the SAW can easily reach from one IDT to another one even without the metal-overlaid waveguides. Test structures of back-to-back IDTs and IDT-taper-taper-IDT structures were also fabricated. The die microphotograph is shown in Fig. 18 and S_{21} for both structures is plotted in Fig. 19. The peak S_{21} of the back-to-back IDT structure is −2.21 dB, while the IDT-taper-taper-IDT structure is −6.77 dB. Based on the two measurements, the loss for a reflector-IDT is about 1.1 dB, while the loss for a taper section is 2.3 dB. It is believed that the mode-conversion loss experienced in the multimode taper region, which is not captured with the use of the monitors in the taper simulation in Fig. 6, along with the larger mass loading effect, which leads to a larger "impedance mismatch" between the IDT and taper regions, is the main contributor to the discrepancy between the calculated loss and the measured loss of the taper region.

B. Waveguide Bends

To conclusively prove the waveguiding action, 180° waveguide bends were used between a pair of IDTs on the same side. The 100-nm aluminum and gold overlay metals were used in these structures. The single-electrode IDT with reflectors was designed for a wavelength of 6 μm, an aperture width of 98.5 μm, and 24 signal-ground finger pairs. The IDT is followed by a 1-mm-long waveguide taper, followed by a 500-μm straight section before connecting to a 180° waveguide bend. A die microphotograph of the waveguide bend test structure is shown in Fig. 20. The measured insertion losses of the entire structure through direct RF probing are shown in Figs. 21 and 22. Fig. 21 shows the plots for waveguide widths of 6 μm and bend radii of 100, 200, and 400 μm, while Fig. 22 shows the insertion loss results for

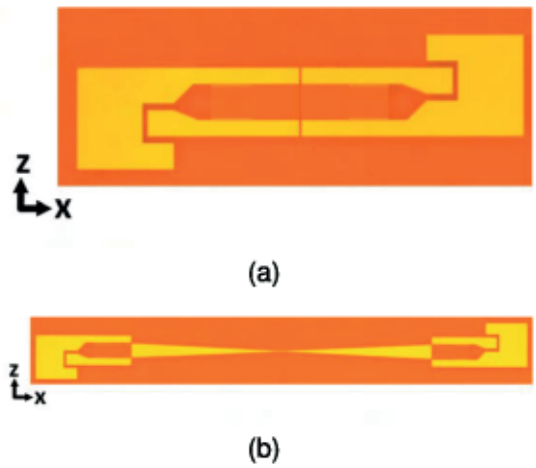

Fig. 18. Die microphotograph for (a) back-to-back IDT test structure and (b) back-to-back IDT-taper structure.

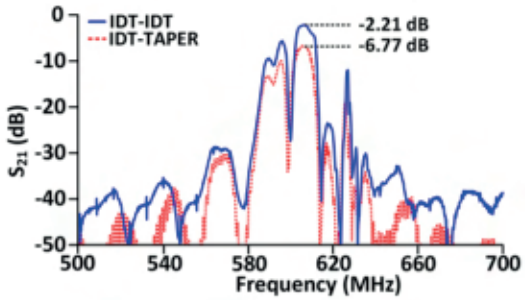

Fig. 19. S_{21} measurement results for back-to-back IDT test structure (blue) and back-to-back IDT-taper structure (red).

Fig. 20. Die microphotograph of the U-bend structures for the outer bend radius of 200 μm and the waveguide width of 6 μm.

waveguide widths of 12 μm for the same bend radii. The peak S_{21} occurs at around 606 MHz for the gold waveguides with peak S_{21} values of −12.5, −9.3, and −9.8 dB for a waveguide width of 6 μm and bending radii of 100, 200, and 400 μm, respectively. The S_{21} measurements of the 180° bend show SAW confinement for the gold waveguide but not for the aluminum waveguide.

To eliminate any doubt about other sources of wave coupling between the IDTs, other than through the waveguides, identical test structures only without the 180° waveguide bend were also fabricated (Fig. 23). The S_{21} measurement results of the test structure without the bend metallization are shown in Fig. 24. The S_{21} difference between the 100-μm bending radius between having and not having the waveguide metallization is about 26 dB, indicating that the waveguide is indeed guiding the SAW through the 180° bend.

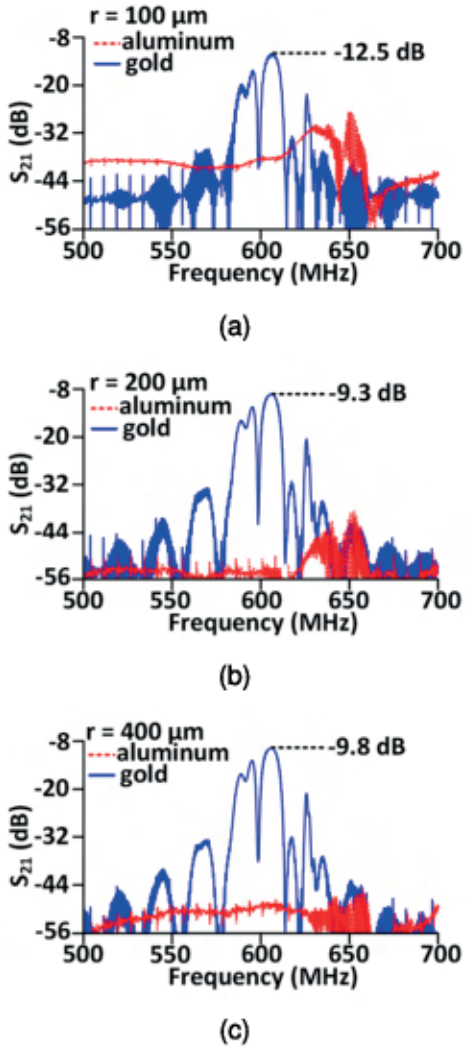

Fig. 21. S_{21} magnitude plots for U-bend test structures. Plots are for a bending radius of (a) 100, (b) 200, and (c) 400 μm for a waveguide width of 6 μm.

C. Waveguide Coupler

A die microphotograph for a waveguide coupler is shown in Fig. 25. Gold metallization is used with a thickness of 100 nm. A 1-mm taper length is used to interface the IDT to the 6-μm-wide waveguide. The gap between the coupled waveguides is 1 μm and the bend radius is 400 μm. The peak S_{21}, S_{31}, and S_{41} are plotted in Fig. 26 for a family of coupling lengths. From the S_{31} and S_{41} results, 100% coupling to the second waveguide occurs around 57 μm and back to the first waveguide at about 190 μm. The waveguide length at which 50% coupling occurs is about 123 μm. The coupling length difference between having 100% of the SAW coupled to the second waveguide and back to the first waveguide is about 133 μm, which matches the simulation results.

D. Electroacoustic Phase Shifter

A die microphotograph of the electroacoustic phase shifter is shown in Fig. 27. The electroacoustic phase shifter was fabricated on a bonded 128° Y-cut $LiNbO_3$-on-Si wafer using 5-nm-thick titanium and 100-nm-thick gold for metallization.

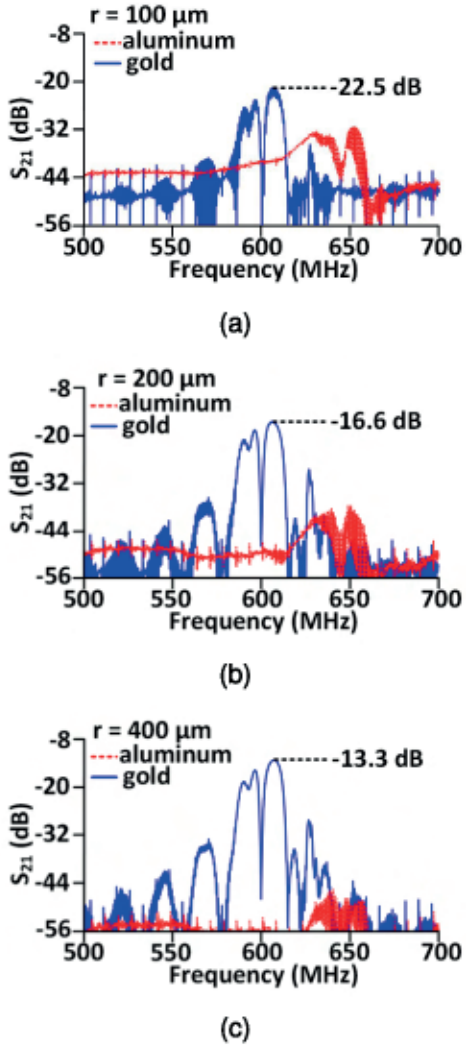

Fig. 22. S_{21} magnitude plots for U-bend test structures. Plots are for a bending radius of (a) 100, (b) 200, and (c) 400 μm for a waveguide width of 12 μm.

Fig. 23. Die microphotograph of the 180° waveguide bend structures without waveguide metallization for an equivalent waveguide outer bend radius of 100 μm.

Single-electrode IDTs with reflectors were designed with a wavelength of 6 μm. Two-port S-parameter measurements were performed using the PNA-X network analyzer through direct RF probing. A dc probe was used to bias the waveguide, while the backside of the die was grounded. The phase shifts were directly measured from the S_{21} phase measurements. The length of the phase shifter, which includes only one of the taper sections, is 6.39 mm. The measured S_{21} magnitude and phase shifts at 612 MHz are shown as the blue curves in Fig. 28.

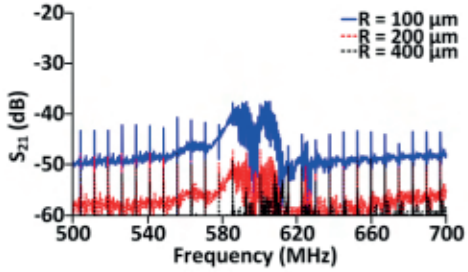

Fig. 24. S_{21} magnitude plots for the 180° waveguide bend test structures without 180° bend metallization for equivalent bend radii of 100, 200, and 400 μm.

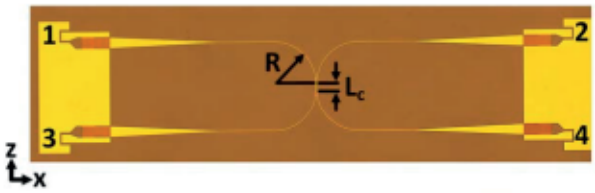

Fig. 25. Die microphotograph of a waveguide coupler. Port numbers are noted by the electrical pads of each port.

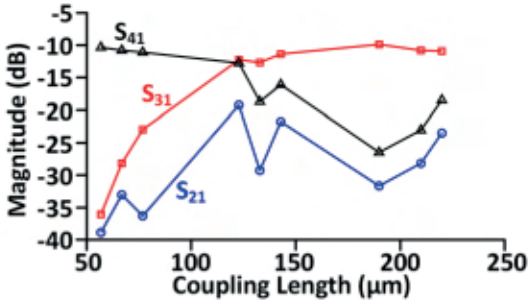

Fig. 26. Peak S_{21}, S_{31}, and S_{41} measurement results for different waveguide coupler coupling lengths.

Fig. 27. Die microphotograph of the electroacoustic phase shifter.

The S_{21} changes by almost 7 dB for the bias voltage range of 0–70 V. Across the entire 70-V bias voltage range, the phase changes by about 510°. Using (8), the SAW velocity changes by about 0.13% to achieve a phase shift of 510°. It is important to note that, unlike the thermal phase shifter, the electroacoustic phase shifter does not consume static dc power while demonstrating a large phase shift.

A 180° waveguide bend structure, similar to the structure shown in Fig. 20 but with a bend radius of 600 μm, was also fabricated on a bonded 128° Y-cut $LiNbO_3$-on-Si wafer. The metallization used was 100-nm-thick gold. The measured S_{21} and phase shifts were measured and plotted as the red curves in Fig. 28. The results demonstrate the electroacoustic

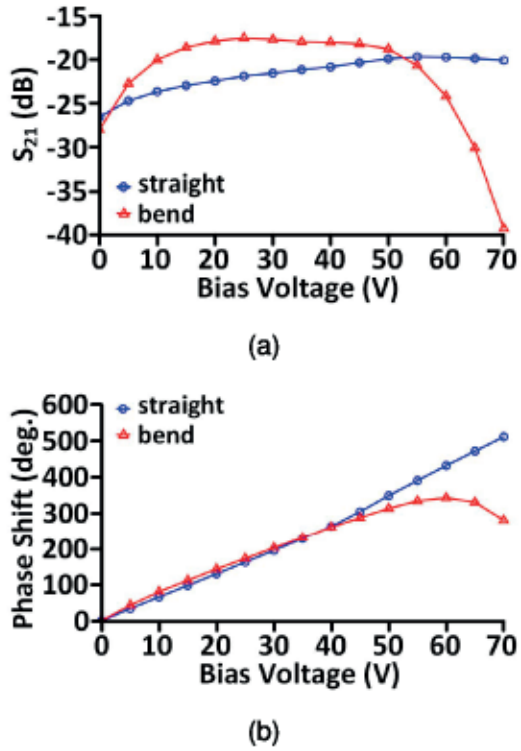

Fig. 28. (a) S_{21} magnitude result and (b) measured phase shifts for the straight SAW phase shifter (blue) and 180° waveguide bend (red) at 609 MHz.

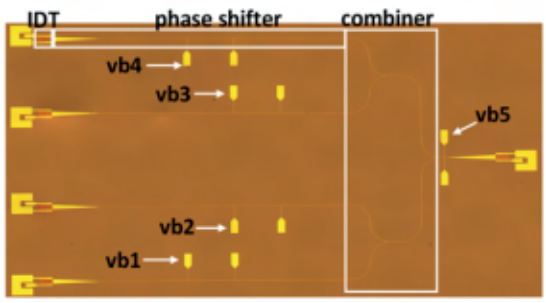

Fig. 29. Die microphotograph of the four-element SAW phased array.

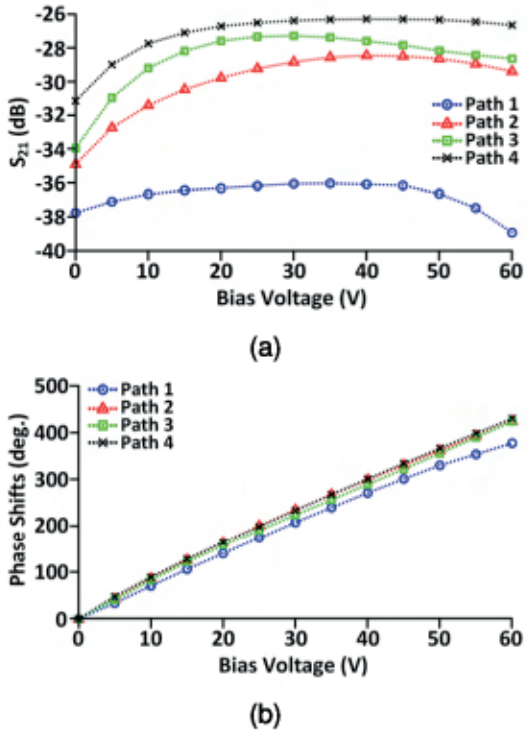

Fig. 30. (a) S_{21} magnitude and (b) phase shifts of the four paths of the SAW phased array at 604 MHz.

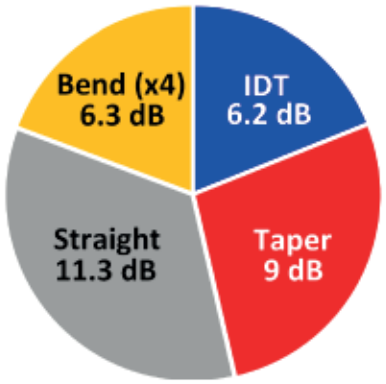

Fig. 31. Estimate of the losses from the different components in the phased array structure.

waveguiding of an SAW through a bend structure as well. Both the straight waveguide and 180° waveguide bend show the loss increasing at higher bias voltages, with the waveguide bend showing a much larger increase. This is believed to be due to the inversion of the surface charges in the silicon behaving as a "short-circuit layer" to the propagating SAW [28].

E. SAW RF Phased Array

The SAW phase shifter was incorporated into a four-element phased array front-end structure (Fig. 29.) The phase shifters are biased through vb1–vb4, with extra pads for redundancy. A binary-tree acoustic waveguide combiner is used to coherently combine the signals from all four paths. The four paths are electrically isolated from each other by a small gap in the waveguide between the phase shifter and the combiner. An additional dc voltage, vb5, is used to bias the waveguides in the combiner to remove excess losses caused by the charges in the silicon surface under the combiner. The die is mounted on a printed circuit board (PCB) using an electrically conductive epoxy and gold wire bonds are used to wire bond the pads to the PCB. The PNA-X network analyzer was used to measure the S-parameters of the array and the S_{21} magnitude and phase of the four different paths at 604 MHz are shown in Fig. 30. While measuring each path individually, the paths that were not being measured were terminated with 50 Ω. Unfortunately, only three out of the four paths were working, and thus, only a three-element phased array can be formed. An estimate of the breakdown of the losses from the different components is shown in Fig. 31. The structures show much larger losses on the electroacoustic platform compared to the non-electroacoustic platform. Biasing the waveguide structures

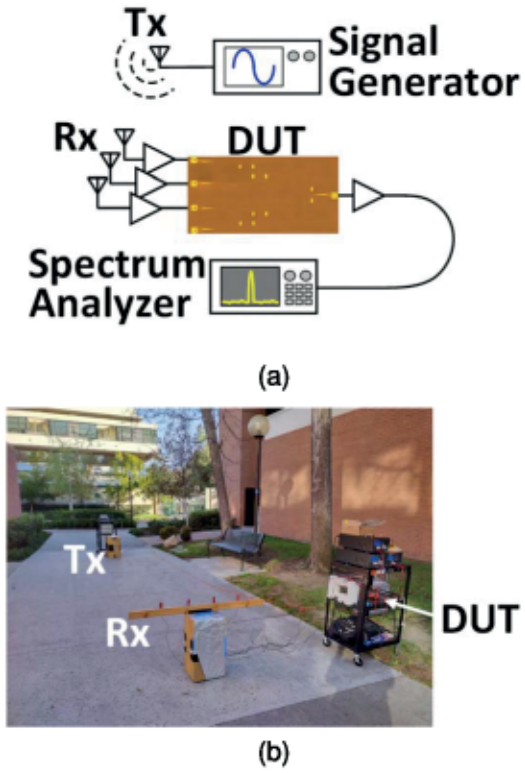

Fig. 32. (a) Diagram of the measurement setup for measuring the antenna pattern of the SAW phased array along with (b) photograph of the outdoor setup.

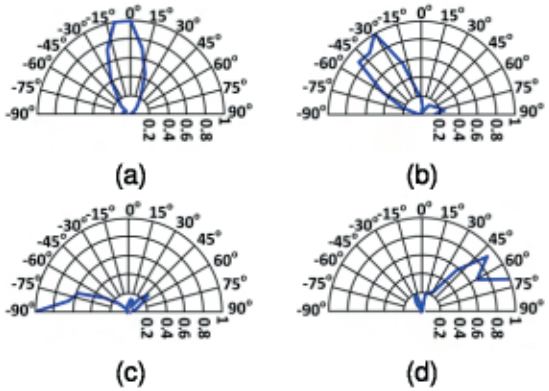

Fig. 33. Measured array pattern for the 3-element SAW phased array for four different settings of (a) –10 degrees, (b) –30 degrees, (c) –90 degrees, and (d) 70 degrees.

helps to reduce the losses, while applying a bias to the IDT structure itself has not shown a noticeable reduction in the loss. The substrate structure as well as the waveguide will need to be further optimized to reduce the loss in order for the structure to be a viable RF front-end solution. For example, optimization of a waveguide bend has shown significant improvements for silicon photonic structures [33]. Similar structure optimizations, as well as inverse design optimizations, can be done to further reduce the taper and waveguide bend losses along with the sizes of these structures [34].

The passive all-acoustic structure can be used both as a phased array Tx and a phased array Rx front end. Outdoor measurements for the all-acoustic phased array front-end chip, connected to antennas, in the receive mode at 604 MHz are presented (Fig. 32). The Tx was kept fixed, while the Rx antennas were rotated around an axis. A Hitite HMC-T2220 synthesized signal generator was used to generate the RF tone for the Tx. The outdoor setup is susceptible to reflections, but beams at four different settings were measured using an Agilent E4407B spectrum analyzer and are shown in Fig. 33. The phased array antenna patterns demonstrate the proper functionality of all the SAW building blocks, namely, straight and bent waveguides, combiners, and electroacoustic phase shifters, in a modestly complex system.

V. Conclusion

We have shown that SAWs can be guided using metal overlaid structures in a process that is compatible with commercial SAW foundries. Gold proves to be a better overlay metal for SAW waveguides when compared to aluminum and tungsten. Design, simulations, fabrication, and measurements of various straight, bent, and coupled waveguide structures realized on 128° Y-cut $LiNbO_3$ were covered. Energy-efficient electroacoustic variable phase shifters were also demonstrated in gold overlaid waveguides that were realized on 128° Y-cut $LiNbO_3$ bonded on a silicon wafer. The electroacoustic variable phase shifters were then used to form an SAW phased array and various angles of beamforming were demonstrated. These studies open up the possibility to realize complex microwave signal processors using SAWs. As a proof-of-concept example, an all-acoustic bidirectional phased array front end is demonstrated. Operation at higher frequencies is possible with better lithography.

Appendix
Fabrication Process

The fabrication of the SAW devices was performed through a conventional liftoff process at the University of Santa Barbara Nanofabrication Facility. The detailed processing steps are given as follows.

1) Solvent clean the $LiNbO_3$-on-Si wafer (single-crystal $LiNbO_3$ wafers).
2) PEII O_2 plasma treatment (wafer surface dehydration): 300 mT/100 W for 1 min.
3) Spin-on LOL2000 underneath resist layer: 2.5 kr/min for 40 s, spun to approximately 200–250 nm thickness.
4) For $LiNbO_3$-on-Si wafers, bake directly on the hot plate at 180 °C for 5 min (for single-crystal $LiNbO_3$ wafers, bake at 160 °C for 5 min with 5 °C/min ramp-up and ramp-down speeds, starting and ending at 50 °C).
5) Spin-on UV6-0.8 top resist layer: 3 kr/min for 30 s to approximately 800 nm thickness.
6) For $LiNbO_3$-on-Si wafers, bake on the hot plate at 135 °C for 1.5 min (for single-crystal $LiNbO_3$ wafers, bake on the hot plate at 135 °C for 1.5 min with 5 °C/min ramp-up and ramp-down speeds).
7) Expose on ASML PAS 5500/300 DUV Stepper at 20-mJ dose, 0-μm focus offset.
8) For $LiNbO_3$-on-Si wafers, post-exposure bake (PEB) at 135 °C for 1.5 min (for single-crystal $LiNbO_3$

wafers, bake on the hot plate at 135 °C for 1.5 min with 5 °C/min ramp-up and ramp-down speeds).

9) Develop in AZ300-MIF developer for 25 s.
10) PEII O_2 plasma descum: 300 mT/100 W for 35 s.
11) E-beam evaporation: Ti/Al = 5 nm/100 nm, Ti/Au = 5 nm/100 nm, and W = 100 nm (no adhesion layer needed).
12) Liftoff in NMP solution cup inside of 80 °C hot-water bath for 2 h, and then, in a fresh NMP solution cup inside of ultrasonic bath at 70 °C for 1 min. Follow with acetone and isopropanol soaking.
13) Spin-on UV-6 resist protective layer to approximately 800 nm thickness (thickness noncritical).
14) For $LiNbO_3$-on-Si wafers, bake on the hot plate at 135 °C for 3 min (for single-crystal $LiNbO_3$ wafers, bake on the hot plate at 135 °C for 3 min with 5 °C/min ramp-up and ramp-down speeds).
15) Dice wafer into chips.
16) Remove photoresist protection with acetone/isopropanol clean.

ACKNOWLEDGMENT

The authors thank Dr. Mina Raiszadeh from JPL for technical feedback in the early stages of this work. A portion of this work was performed at the UCSB Nanofabrication Facility, an open-access laboratory.

REFERENCES

[1] C. K. Campbell, *Surface Acoustic Wave Devices and Their Signal Processing Applications*. San Diego, CA, USA: Academic, 1989.
[2] D. Morgan, *Surface Acoustic Wave Filters With Applications to Electronic Communications and Signal Processing*, 2nd ed. Amsterdam, The Netherlands: Academic, 2007.
[3] M. Lewis, "Surface acoustic wave devices and applications: 6. Oscillators—The next successful surface acoustic wave device?" *Ultrasonics*, vol. 12, no. 3, pp. 115–123, 1974.
[4] C. K. Campbell, "Surface acoustic wave convolvers for spread-spectrum mobile and wireless communications," in *Proc. Int. Symp. Electromagn. Compat.*, May 1999, pp. 686–689.
[5] F. Marshall and E. Paige, "Novel acoustic-surface-wave directional coupler with diverse applications," *Electron. Lett.*, vol. 7, no. 18, pp. 460–462, Aug. 1971.
[6] B. R. Potter, "Surface acoustic wave slanted correlators for linear FM pulse-compressors," in *IEEE MTT-S Int. Microw. Symp. Dig.*, Jun. 1977, pp. 318–320.
[7] P. Delsing et al., "The 2019 surface acoustic waves roadmap," *J. Phys. D, Appl. Phys*, vol. 52, no. 35, Jul. 2019, Art. no. 353001.
[8] D. M. Pozar, *Microwave Engineering*, 3rd ed. Hoboken, NJ, USA: Wiley, 2005.
[9] S. Idres and H. Hashemi, "Optical binary switched delay line based on low loss multimode waveguide," in *Proc. Opt. Fiber Commun. Conf. (OFC)*, 2022, pp. 1–3.
[10] R. Lu, T. Manzaneque, Y. Yang, and S. Gong, "S0-mode lithium niobate acoustic delay lines with 1 dB insertion loss," in *Proc. IEEE Int. Ultrason. Symp.*, Oct. 2018, pp. 1–9.
[11] J. Zhou et al., "Integrated full duplex," *IEEE Commun. Mag.*, vol. 55, pp. 142–151, Apr. 2017.
[12] E. A. Ash, R. M. De La Rue, and R. F. Humphryes, "Microsound surface waveguides," *IEEE Trans. Microw. Theory Techn.*, vol. MTT-17, no. 11, pp. 882–892, Nov. 1969.
[13] A. A. Oliner, "Waveguides for acoustic surface waves: A review," *Proc. IEEE*, vol. 64, no. 5, pp. 615–627, May 1976.
[14] L. R. Adkins and A. J. Hughes, "Long delay lines employing surface acoustic wave guidance," *J. Appl. Phys.*, vol. 42, no. 5, pp. 1819–1822, Apr. 1971.
[15] L. R. Adkins and A. J. Hughes, "Acoustic surface wave directional couplers," in *IEEE GMTT Int. Microw. Symp. Dig*, May 1970, pp. 375–379.
[16] E. A. Ash and D. Morgan, "Realisation of microwave-circuit functions using acoustic surface waves," *Electron. Lett.*, vol. 3, no. 10, pp. 462–464, Oct. 1967.
[17] R. A. Waldron, "Microsound waveguides and waveguide components," *IEEE Trans. Sonics Ultrason.*, vol. SU-18, no. 4, pp. 219–230, Oct. 1971.
[18] L. Shao et al., "Electrical control of surface acoustic waves," Jan. 2021, *arXiv:2101.01626*.
[19] J. Tsutsumi, T. Matsuda, O. Ikata, and Y. Satoh, "A novel reflector-filter using a SAW waveguide directional coupler," *IEEE Trans. Ultrason., Ferroelectr., Freq. Control*, vol. 47, no. 5, pp. 1228–1234, Sep. 2000.
[20] P. Boucher, S. Rauwerdink, A. Tahraoui, C. Wenger, Y. Yamamoto, and P. V. Santos, "Ring waveguides for gigahertz acoustic waves on silicon," *Appl. Phys. Lett.*, vol. 105, no. 16, Oct. 2014, Art. no. 161904.
[21] B. Lee, S. Lee, H. Lee, and H. Shin, "Young's modulus measurement of aluminum thin film with cantilever structure," *Proc. SPIE*, vol. 4557, pp. 225–232, Sep. 2001.
[22] F. Zhu, Z. Xie, and Z. Zhang, "Phase control and Young's modulus of tungsten thin film prepared by dual ion beam sputtering deposition," *AIP Adv.*, vol. 8, pp. 1–7, Mar. 2018.
[23] C. Birleanu et al., "Temperature effect on the mechanical properties of gold nano films with different thickness," in *Proc. IOP Conf. Mater. Sci. Eng.*, vol. 147, Aug. 2016, Art. no. 012021.
[24] L. Chrostowski and M. Hochberg, *Silicon Photonics Design*. Cambridge, U.K.: Cambridge Univ. Press, 2015.
[25] R. B. Ward, "Temperature coefficients of SAW delay and velocity for Y-cut and rotated $LiNbO_3$," *IEEE Trans. Ultrason., Ferroelectr., Freq. Control*, vol. 37, no. 5, pp. 481–483, Sep. 1990.
[26] N. Harris et al., "Efficient, compact and low loss thermo-optic phase shifter in silicon," *Opt. Exp.*, vol. 22, pp. 10487–10493, May 2014.
[27] J. D. Crowley, J. F. Weller, and T. G. Giallorenzi, "Acoustoelectric SAW phase shifter," *Appl. Phys. Lett.*, vol. 31, no. 9, pp. 558–560, Nov. 1977.
[28] S. Urabe, "Voltage controlled monolithic SAW phase shifter and its application to frequency variable oscillator," *IEEE Trans. Sonics Ultrason.*, vol. SU-29, no. 5, pp. 255–261, Sep. 1982.
[29] S. Zhang et al., "Surface acoustic wave devices using lithium niobate on silicon carbide," *IEEE Trans. Microw. Theory Techn.*, vol. 68, no. 9, pp. 3653–3666, Sep. 2020.
[30] B. G. Streetman and S. K. Banerjee, *Solid State Electronic Devices*, 7th ed. London, U.K.: Pearson, 2015.
[31] J. Zhu, Y. Chen, G. Saraf, N. Emanetoglu, and Y. Lu, "Voltage tunable surface acoustic wave phase shifter using semiconducting/piezoelectric ZnO dual layers grown on r-Al_2O_3," *Appl. Phys. Lett.*, vol. 89, pp. 1–3, Sep. 2006.
[32] H. Jiang and X. Ruimin, "X-band 3D meander stripline delay line using multilayer LTCC," in *IEEE MTT-S Int. Microw. Symp. Dig.*, Jun. 2009, pp. 345–348.
[33] M. Nakai, T. Nomura, S. Chung, and H. Hashemi, "Geometric loss reduction in tight bent waveguides for silicon photonics," in *Proc. Conf. Lasers Electro-Opt.*, May 2018, pp. 1–2.
[34] Z. Li et al., "Ultra-compact high efficiency and low crosstalk optical interconnection structures based on inverse designed nanophotonic elements," *Sci. Rep.*, vol. 10, pp. 1–9, Jul. 2020.